Magnons reveal topology and dynamics of a skyrmion crystal

R. Ayache[†], [1]N. Chakraborti[†], [2]M. Kuiri,[1,3] Q. Benichou,[1] H. Chakraborti,[1,4] L. Pugliese,[1] K. Watanabe,[5] T. Taniguchi,[5] R. Moessner,[6] B. Doucot,[7] and P. Roulleau[*1]

[1]*SPEC, CEA, CNRS, Université Paris-Saclay, CEA Saclay, 91191 Gif sur Yvette Cedex France*
[2]*TCM Group, Cavendish Laboratory, University of Cambridge, Cambridge CB3 0HE, United Kingdom*
[3]*Department of Physics, Birla Institute of Technology and Science, Pilani, Hyderabad Campus, Jawahar Nagar, Kapra Mandal, Medchal District, Telangana 500078, India*
[4]*4Laboratory of Atomic and Solid State Physics, Cornell University, Ithaca 14850, NY, USA*
[5]*National Institute for Materials Science, 1-1 Namiki, Tsukuba, 305-0044, Japan*
[6]*Max-Planck Institut für Physik komplexer Systeme, Nöthnitzer Straße 38, Dresden 01187, Germany*
[7]*LPTHE, UMR 7589, CNRS and Sorbonne Université, 75252 Paris Cedex 05, France*

†: equal contribution
*Corresponding author: preden.roulleau@cea.fr

MATERIALS AND METHODS

Device Fabrication and geometry

High-quality hBN/graphene/hBN/graphite heterostructures were prepared via mechanical exfoliation followed by a dry transfer method. Monolayer graphene and few-layer graphite were obtained by exfoliating natural graphite (NGS GmbH) onto pre-cleaned Si/SiO_2 substrates with a 285 nm oxide layer. In a similar manner, hexagonal boron nitride (hBN) flakes were exfoliated from bulk hBN crystals (NIMS, Japan) onto separate cleaned Si/SiO_2 substrates. The exfoliated flakes were initially characterized using optical microscopy. To assess flake uniformity and imperfections, dark-field and differential interference contrast imaging were employed. Flakes exhibiting uniform contrast and absence of visible cracks were selected for further inspection. These selected flakes were subsequently characterized using non-contact mode atomic force microscopy (AFM) to verify surface quality, ensure the absence of microcracks or surface contamination, and confirm thickness uniformity across the flake. A suitable graphite flake was selected and transferred onto a pre-patterned p-doped Si/SiO_2 substrate using a polypropylene carbonate (PC)/polydimethylsiloxane (PDMS) stamp. The graphite flake was then patterned into two independent local bottom gates denoted as left and right gate using electron beam lithography (EBL) followed by oxygen plasma etching. The two gate regions were separated by a narrow constriction slit approximately 70 nm wide, as shown in Fig. S1a. Following the patterning, the graphite flake was cleaned in hot acetone for several hours to remove resist residues, and then annealed under vacuum at 350°C to eliminate surface contaminants. The patterned structure was again examined using non-contact AFM to ensure the uniformity of the flake. Next, a van der Waals heterostructure consisting of monolayer graphene encapsulated between two hexagonal boron nitride (hBN) layers (∼37 nm thick on top and ∼60 nm at the bottom) was assembled and aligned precisely over the pre-patterned graphite gates using the PC/PDMS stamp. The stack was then cleaned, followed by vacuum annealing at 350°C to remove polymer residues and improve interfacial cleanliness. The fabricated stack was subsequently patterned using EBL and reactive ion etching (RIE) with CHF_3/O_2 gas to shape the graphene. A second EBL step was performed to design one-dimensional edge contacts, followed by another CHF_3/O_2 RIE step to selectively etch and expose the graphene edges. The contacts were made in a finger-like geometry to increase the contact area and reduce the contact resistance. Cr/Au (10/70 nm) was deposited by electron beam evaporation at an angle using a tilted stage to ensure sidewall coverage. The graphene channel was subsequently defined through an additional EBL step and etched using the same RIE recipe. An optical image of the completed device is presented in Fig. S1b and a schematic of the heterostructure stack is shown in Fig. S1c.

The device comprises two local graphite gates, which define a lateral junction across the graphene channel. On the left side, the graphene contacts lie entirely within the bottom-gated region, whereas on the right side, the graphene contacts extend beyond the local gate and partially reside on the SiO_2/Si substrate (Fig. S1c). This design enables electrostatic doping of the extended contact region via the global Si back gate, effectively reducing contact resistance on the right side and enabling control over magnon emission. Fig. S2 shows an optical image of the device, highlighting the constriction and gate geometry. The graphene channel and both local gates have widths of 0.6 μm, and the separation between the left and right gates is 70 nm.

Transport Measurements

Transport measurements were conducted using an Oxford Instruments Proteox dilution refrigerator with a base temperature of approximately 10 mK and a magnetic field of up to 14 T applied perpendicular to the sample plane. Standard low-frequency lock-in techniques were employed to probe the electrical response of the device. An excitation current in the range of 1–5 nA was applied using a Stanford Research Systems SR830 lock-in amplifier, with modulation frequencies varied between 7 Hz and 217 Hz to optimise signal to noise conditions across different measurement regimes. The output voltage signal was amplified using a low-noise, high-impedance preamplifier (input impedance ∼100 MΩ). All electrical lines were filtered using low-pass RC filters, and were thermally anchored at multiple stages within the cryostat to suppress spurious heating and minimise electronic noise.

Experimental details

Quantum Hall Transport Characteristics

To assess the quality of the device and establish the robustness of the quantum Hall regime in our junction geometry, we first characterize the Hall response as a function of magnetic field and carrier density. Figure S4a shows a Landau fan of the transverse resistance R_{xy}, measured in a two-terminal configuration while sweeping the right gate voltage between 6 and 13 T. A constant series resistance of 750 Ω—corresponding to the contact resistance of the measurement line—has been subtracted from all traces. Well-developed quantum Hall plateaux appear at $\sigma_{xy} = e^2/3h$, $2e^2/3h$, e^2/h, and $2e^2/h$. The observation of fractional plateaux demonstrates the high mobility and low disorder of the sample. Figure S4b displays representative line cuts of R_{xy} at fixed magnetic fields (6, 7.75, 9.5, 11.25, and 13 T).

To further probe the stability of the integer states, we examine the breakdown of the $\nu = 1$ quantum Hall plateau. Figure S4c shows the bias dependence of the $\nu = 1$ state. The plateau remains quantized up to moderate bias, but a small decrease of 2.5–8% is observed at $V_{\mathrm{ds}} = 20$ mV, signaling the onset of dissipative processes prior to full breakdown. Representative cuts in Fig. S4d illustrate the breakdown of the $\nu = 1$ state. The well-quantized Hall plateaux indicate that the bulk is largely incompressible over the measured gate and field range, providing a clean environment for magnon propagation.

Together, these results confirm that the device enters a well-developed integer quantum Hall regime with robust plateaux, demonstrating a largely incompressible bulk that provides a clean platform for investigating magnon propagation and electrically tunable scattering across the junction.

Magnon emission and detection mechanism

A schematic of the electrical pathways for magnon emission and detection is shown in Figure S3. The sample is first tuned into the $\nu = 1$ quantum Hall ferromagnetic state by applying appropriate voltages to the two halves of the bottom gate at a perpendicular magnetic field of 13 T. In this regime, a single spin-polarized chiral edge channel runs along the sample boundary. Near the metallic contacts, however, local doping raises the filling factor, creating an additional inner edge channel of opposite spin polarization. Because these two edge modes carry opposite spins, elastic scattering between them is forbidden unless the energy imbalance exceeds the Zeeman energy $E_Z = g\mu_B B$.

A voltage (V_{ds}) is applied to a contact denoted as 'Em'. Because only spin-down angular momentum can enter and propagate through the spin-up bulk of the quantum Hall ferromagnet, magnons are generated at the position marked with a minus sign(⊖) when the chemical potential of the inner edge satisfies $\mu \geq E_Z$ with respect to the outer edge. Conversely, for positive V_{ds}, magnon creation occurs at the position marked with a plus sign. Once generated, these magnons propagate through the insulating QH ferromagnet and can be absorbed at remote edge channels through the reverse spin-flip process. Such magnon absorption changes the conductance of the distant edge channel, enabling nonlocal detection of magnon transport.

Influence of the Electric Field

To examine how the in-plane electric field affects magnon propagation across the junction, we emit magnons from three contacts ($E_{\mathrm{m},1}$, $E_{\mathrm{m},2}$, and $E_{\mathrm{m},3}$) arranged as shown in Fig. S5a and detect the resulting non-local response at NL2. For clarity the schematic depicts all emitters simultaneously, but in the experiment each dataset was obtained independently by activating only a single emitter at a time. The strongest non-local signal is observed for the lateral emitters $E_{\mathrm{m},1}$ and $E_{\mathrm{m},3}$, whose emission directions intersect the junction at oblique angles. In this geometry, the magnons acquire a larger transverse momentum component q_y, which increases the effective dipolar moment associated with their precession and strengthens the coupling between their electric dipole $\mathbf{p}$ and the in-plane electric field E_x across the junction. Because the dipole–field interaction scales as $\mathbf{p} \cdot \mathbf{E}$, magnons with finite q_y experience a stronger field-induced torque than those approaching the junction nearly normal to it. This enhanced coupling promotes elastic mode mixing and trajectory bending within the junction region, effectively redirecting magnons and increasing their probability of being absorbed or detected at NL2. In addition, the field can transfer spectral weight from long-lived propagating modes into more strongly damped modes, further reducing the transmitted magnon population.

Additional attenuation may originate from the electrostatic disorder, where localized charge puddles create spatially varying electric fields and modifications of the local magnetic environment. Although magnons are charge-neutral, their dipolar nature renders them sensitive to these gradients, leading to additional scattering, deflection, or partial absorption before they reach NL2.

Magnon propagation and Signal Conservation at $\nu_L = 1 - \varepsilon$

As a complement to the measurements performed at $\nu_L = 1 + \varepsilon$, which correspond to most of the data presented in the main text, we also investigate magnon propagation slightly below the integer filling, at $\nu_L = 1 - \varepsilon$. To probe this regime, we excite the central emitter $E_{\mathrm{m},2}$ and measure the resulting non-local signals at all three detectors, NL1, NL2, and NL3 (Fig. S6a). The measurements are performed while simultaneously recording the Hall conductivity σ_{xy} of the right-gated region (Fig. S6b), providing a reference for the local electronic state.

The non-local signals at the three detectors show a remarkable feature: although individual detector amplitudes vary slightly due to geometric factors and small residual disorder, the total integrated signal summed over NL1, NL2, and NL3 remains approximately constant (Fig. S6c). This conservation implies that the magnons emitted from $E_{\mathrm{m},2}$ propagate through the bulk without significant loss or absorption, consistent with a high-quality, incompressible bulk state.

From this measurement perspective, we do not observe any distinctive signatures of a skyrmion crystal in the bulk: the magnon signal distribution remains smooth and conserved, without strong spatial modulation or anomalous enhancement that might indicate a skyrmion lattice.

Dipole moment -electric field picture and non-linear sigma model: Two semiclassical limits

Dipole picture

This description first arose in the early paper by Kallin and Halperin [1] and it is based on the following Hamiltonian:

$$H_{\mathrm{eff}}(\boldsymbol{r},\boldsymbol{q}) = \sqrt{\frac{\pi}{32}}\frac{e^2}{\epsilon l_B}(ql_B)^2 + V_{\mathrm{ext}}(\boldsymbol{r} + \frac{l_B^2}{2}\boldsymbol{z}\times\boldsymbol{q}) - V_{\mathrm{ext}}(\boldsymbol{r} - \frac{l_B^2}{2}\boldsymbol{z}\times\boldsymbol{q}) \tag{1}$$

where the first term is the standard one derived in [1] for a magnon on top of a ferromagnetic background, and the second two arise in the presence of an external electrostatic potential, induced for example by gating the 2D electron gas. In this equation, $\boldsymbol{r}$ denotes the center of mass position of the dipole formed by a spin-carrying particle-hole pair, and q is the conjugate wave-vector. A key insight of [1] is that the relative coordinate of the dipole $\boldsymbol{s} = \boldsymbol{r}_{\mathrm{part}} - \boldsymbol{r}_{\mathrm{hole}}$ is directly related to the momentum $\boldsymbol{q}$ according to $\boldsymbol{q} = l_B^2\boldsymbol{z}\times\boldsymbol{q}$. Microscopically, this arises because all single particle orbital degrees of freedom are constrained to belong to a single Landau level. Because guiding center coordinates for a single electron behave as a pair of canonically conjugate variables, the classical phase-space associated to a particle-hole pair is four-dimensional, and can be organized in terms of the $\boldsymbol{r},\boldsymbol{q}$ pair. The precise status of $H_{\mathrm{eff}}(\boldsymbol{r},\boldsymbol{q})$ is as the Weyl symbol of the Hamiltonian operator $\hat{H}$ acting on the subspace of electronic Fock space corresponding to a single particle-hole pair. If $\Psi(\boldsymbol{r})$ denotes the wave-function, then:

$$(\hat{H}\Psi)(\boldsymbol{r}) = \int \frac{d^2\boldsymbol{r'}d^2\boldsymbol{q}}{(2\pi)^2} H_{\mathrm{eff}}(\frac{\boldsymbol{r}+\boldsymbol{r'}}{2},\boldsymbol{q})\, e^{i\boldsymbol{q}.(\boldsymbol{r}-\boldsymbol{r'})}\,\Psi(\boldsymbol{r'}) \tag{2}$$

In this work, we are not attempting to solve the associated time-dependent Schrödinger equation for such dipole wave-functions, but limit ourselves to semi-classical equations of motion for localized wave-packets. This is valid in the short wave-length limit $1 \ll qd_{\mathrm{ext}}$, where d_{ext} stands for the characteristic length of the spatial variations of V_{ext}. The equations of motion for the phase-space location of wave-packets take the usual Hamiltonian form: $\hbar\frac{d\boldsymbol{r}}{dt} = \boldsymbol{\nabla}_{\boldsymbol{q}}H_{\mathrm{eff}}$, $\hbar\frac{d\boldsymbol{q}}{dt} = -\boldsymbol{\nabla}_{\boldsymbol{r}}H_{\mathrm{eff}}$. These equations become much simpler in the limit when the separation s between the particle and the hole is small compared to d_{ext}, so that we can replace $V_{\mathrm{ext}}(\boldsymbol{r}_{\mathrm{part}}) - V_{\mathrm{ext}}(\boldsymbol{r}_{\mathrm{hole}})$ by $l_B^2(\boldsymbol{z}\times\boldsymbol{q}).\boldsymbol{\nabla}V_{\mathrm{ext}}(\boldsymbol{r})$. This requires the following upper bound on the momentum: $ql_B^2 \ll d_{\mathrm{ext}}$. In order for this upper bound to be compatible with the previous lower bound, we require that $l_B \ll d_{\mathrm{ext}}$, which we assume to be valid throughout this work.

Non-linear sigma model picture

The dipole picture has been firmly established for magnon propagation through a ferromagnetic background. In the presence of skyrmions, it is probably easier to start from a description based on the non-linear sigma model [2, 3]. It is based on the Lagrangian:

$$L = \hbar\int \frac{d^2\boldsymbol{r}}{4\pi l_B^2}\,\boldsymbol{\mathcal{A}}(\boldsymbol{n}).\partial_t\boldsymbol{n} - H, \tag{3}$$

where $\boldsymbol{\nabla} \times \boldsymbol{\mathcal{A}}(\boldsymbol{n}) = \boldsymbol{n}$, and the energy functional H is given by:

$$H = \frac{\rho_s}{2} \int (\boldsymbol{\nabla} \boldsymbol{n})^2 + \frac{e^2}{2\epsilon} \int d^2\boldsymbol{r} d^2\boldsymbol{r'} \, \frac{Q(\boldsymbol{r}) Q(\boldsymbol{r'})}{|\boldsymbol{r} - \boldsymbol{r'}|} + \int d^2\boldsymbol{r} \, V_{\rm ext}(\boldsymbol{r}) \, Q(\boldsymbol{r}) \tag{4}$$

In this expression, the stiffness $\rho_s = e^2/16\sqrt{2\pi}\epsilon l_B$, and the topological charge density is given by:

$$Q(\mathbf{r}) = \frac{1}{4\pi} \mathbf{n} \cdot (\partial_x \mathbf{n} \times \partial_y \mathbf{n}) \ . \tag{5}$$

The resulting equations of motion take the usual Landau-Lifschitz form:

$$\frac{\partial \boldsymbol{n}}{\partial t} = \frac{4\pi l_B^2}{\hbar} \, \boldsymbol{z} \times \boldsymbol{\nabla}_{\boldsymbol{n}(\boldsymbol{r})} H \tag{6}$$

In the case of a ferromagnetic background, the connection between the non-linear sigma model description and the dipole picture can be understood as follows. Assuming that spins point everywhere close to the north pole, the spin texture can be described via the small planar components $n_x(\boldsymbol{r}), n_y(\boldsymbol{r}) \ll 1$. In a quantum description, this corresponds to a local spin-1/2 wave-function $(\Psi_\uparrow(\boldsymbol{r}), \Psi_\downarrow(\boldsymbol{r})) \simeq (1, (n_x(\boldsymbol{r}) + i n_y(\boldsymbol{r}))/2)$, neglecting second order terms in $n_x(\boldsymbol{r})$ and $n_y(\boldsymbol{r})$. In this situation, the dipole wave-function $\Psi(\boldsymbol{r})$ can be identified with $\Psi_\downarrow(\boldsymbol{r})$, so the time dependent Schrödinger equation for $\Psi(\boldsymbol{r})$ translates into the linearized Landau-Lifschitz equation of motion for the in plane spin deviations $(n_x(\boldsymbol{r}), n_y(\boldsymbol{r}))$. It is instructive to check this statement by considering the effect of an external potential $V_{\rm ext}(\boldsymbol{r})$. The linearized equations of motion can be obtained by considering the second order variation of H around an equilibrium configuration. When the latter is the ferromagnetic state along the north pole, we get, setting $\Psi(\boldsymbol{r}) = 2\Psi_\downarrow(\boldsymbol{r})$:

$$H = \frac{\rho_s}{2} \int |\boldsymbol{\nabla} \Psi|^2 + \frac{i}{8\pi} \int V_{\rm ext} \, (\partial_x \Psi \, \partial_y \bar{\Psi} - \partial_y \Psi \, \partial_x \bar{\Psi}) \tag{7}$$

This leads to:

$$i\hbar \frac{\partial \Psi}{\partial t} = -\sqrt{\frac{\pi}{32}} \frac{e^2}{\epsilon l_B} (l_B \boldsymbol{\nabla})^2 \Psi + \frac{l_B^2}{2i} \, \boldsymbol{z}.(\boldsymbol{\nabla} \Psi \times \boldsymbol{\nabla} V_{\rm ext})(\boldsymbol{r}) \tag{8}$$

Setting $\hat{q} = -i\boldsymbol{\nabla}$, and in the long wave-length limit ($q l_B^2 \ll d_{\rm ext}$), we recover the Schrödinger equation associated to the Hamiltonian operator (1) acting on the dipole wave-function $\Psi(\boldsymbol{r})$.

In the presence of a slowly varying spin texture, the magnon dynamics is modified due to the presence of a spin Berry phase induced by spatial gradients of the spin orientation. This manifests as an additional orbital magnetic field, equal to the topological charge density $4\pi \, Q(\boldsymbol{r})$ acting on a magnon [4]. As usual, we take this effect into account by substituting the covariant derivative $-i\boldsymbol{\nabla} - \boldsymbol{A}$ to the original $-i\boldsymbol{\nabla}$ operator, where $\boldsymbol{\nabla} \times \boldsymbol{A} = 4\pi \, Q$. Because skyrmions are charged objects, they generate an additional electrostatic potential, therefore the external potential has to be replaced in the magnon equation of motion by the local potential:

$$V_{\rm loc}(\boldsymbol{r}) = V_{\rm ext}(\boldsymbol{r}) + \frac{e^2}{\epsilon} \int d^2\boldsymbol{r'} \, \frac{Q(\boldsymbol{r'})}{|\boldsymbol{r} - \boldsymbol{r'}|} \tag{9}$$

In the following, it will be convenient to use rescaled space-time coordinates, where the position is expressed in units of l_B and $\boldsymbol{p}$ stands for $l_B \boldsymbol{q}$. Since we are working in the geometrical optics approximation for the magnons, we describe them by a wave-packet of the form:

$$\Psi(\boldsymbol{r}) = \theta \, e^{-\frac{(\boldsymbol{r} - \boldsymbol{r}_m)^2}{2a^2}} \, e^{i(\boldsymbol{p}.(\boldsymbol{r} - \boldsymbol{r}_m) + \varphi)} \tag{10}$$

where $\boldsymbol{r}_m$ denotes the magnon position and $\boldsymbol{p}$ its momentum, θ is the amplitude of the spin deviation away from the average magnetization vector, and φ a global phase. The spatial scale a is chosen to be large compared to p^{-1} and small compared to the characteristic scales associated to the variations of the local potential. Inserting this Ansatz in the above energy functional (7), adapted to the case of slowly varying texture as explained above, gives:

$$(\theta^2 \pi a^2)^{-1} H(\boldsymbol{r}_m, \boldsymbol{p}, \theta) = \frac{\rho_s}{2} \left((\boldsymbol{p} - \boldsymbol{A})^2 - 4\pi \, Q_0(\boldsymbol{r}) \right) + \frac{\hat{\boldsymbol{z}}}{8\pi}.((\boldsymbol{p} - \boldsymbol{A}) \times \boldsymbol{\nabla} V_{\rm loc}) - \frac{1}{2} \, V_{\rm loc}(\boldsymbol{r}) \, Q_0(\boldsymbol{r}) \tag{11}$$

So far, the amplitude of the spin deviation θ and the size a of the wave-packet are undetermined. To lift this indeterminacy, we notice that the total magnetization in the system is given by:

$$\boldsymbol{M} = \int \frac{d^2\boldsymbol{r}}{2\pi}\, \boldsymbol{n}(\boldsymbol{r}) \tag{12}$$

We now impose that, when applied on a ferromagnetic background, introducing a magnon wave-packet produces the same total magnetization as flipping one local spin into its opposite. This leads to:

$$2 = \int \frac{d^2\boldsymbol{r}}{2\pi}\, (1 - \sqrt{1 - |\Psi(\boldsymbol{r})^2|}) \tag{13}$$

Assuming that θ is small and performing the gaussian integral gives:

$$\theta^2 \pi a^2 = 8\pi \tag{14}$$

Inserting this value in the above expression (11) gives the following magnon Hamiltonian

$$H_{\rm mag} = \frac{\omega_{\rm int}}{2}\Big(\big(p_x - A_x\big)^2 + \big(p_y - A_y\big)^2 \Big) + \big(p_x - A_x\big)\, \partial_y V_{\rm loc} - \big(p_y - A_y\big)\, \partial_x V_{\rm loc} \tag{15}$$

where $\omega_{\rm int} = \sqrt{\pi/8}\, e^2/(\hbar\epsilon l_B)$. To simplify the notation, the magnon position is denoted here by $\boldsymbol{r}$ instead of $\boldsymbol{r}_m$. Note that we have neglected the potential terms in (11) since the most interesting physical effects on magnon propagation are due to the presence of the effective orbital magnetic field $\boldsymbol{A}$ [4] and of a dipole moment proportional to the linear momentum and orthogonal to it [1]. The corresponding Hamiltonian equations of motion read:

$$\frac{d\boldsymbol{r}}{dt} = \boldsymbol{\nabla}_{\boldsymbol{p}} H_{\rm mag}, \quad \frac{d\boldsymbol{p}}{dt} = -\boldsymbol{\nabla}_{\boldsymbol{r}} H_{\rm mag} \tag{16}$$

From the above Hamiltonian, one can apply a Legendre transform to obtain the Lagrangian:

$$L_{\rm mag} = \frac{1}{2\omega_{\rm int}} \big((\dot{x} - v_x)^2 + (\dot{y} - v_y)^2 \big) + A_x \dot{x} + A_y \dot{y}, \tag{17}$$

where we have introduced the drift velocity (v_x, v_y) defined by $v_x = \partial_y V_{\rm loc}$ and $v_y = -\partial_x V_{\rm loc}$. The equations of motion take the form:

$$\begin{aligned} \ddot{x} &= \omega_{\rm int} \left(\partial_x A'_y - \partial_y A'_x\right) \dot{y} + \frac{1}{2}\partial_x \big(v_x^2 + v_y^2\big) \\ \ddot{y} &= -\omega_{\rm int} \left(\partial_x A'_y - \partial_y A'_x\right) \dot{x} + \frac{1}{2}\partial_y \big(v_x^2 + v_y^2\big) \end{aligned} \tag{18}$$

where $A'_x = A_x - v_x/\omega_{\rm int}$ and $A'_y = A_y - v_y/\omega_{\rm int}$. We see that there are two Lorentz force contributions, one arising from the twist of the spin and the corresponding Berry phase, and the other due to the drift velocity induced by the smooth variation of the external potential. The latter also gives rise to an effective scalar potential.

So far, we have discussed magnon dynamics around a fixed texture. However, in the presence of a finite region containing a Skyrmion crystal, we have two types of low energy excitations: unbound ones, that may be injected far away from the Skyrmion crystal and may propagate to arbitrary distances, and internal breathing modes of the crystal. For simplicity, we shall consider only the breathing modes. These can be parametrized by N_S Skyrmion positions $\boldsymbol{R}_1, ..., \boldsymbol{R}_{N_S}$, so that the above Hamiltonian dynamics associated to one magnon has to be extended to incorporate these magneto-phonon degrees of freedom. Concretely, this implies that the reference spin texture should now be regarded as a function $\boldsymbol{n}(\boldsymbol{r}; \boldsymbol{R}_1, ...\boldsymbol{R}_{N_S})$ of $N_S + 1$ positions. In an adiabatic picture, we can in principle minimize the non-linear sigma model energy functional in the presence of the external potential $V_{\rm ext}$ with the constraint that N_S Skyrmions are centered at $\boldsymbol{R}_1, ..., \boldsymbol{R}_{N_S}$, so that we get an energy function $V_{\rm el}(\boldsymbol{R}_1, ..., \boldsymbol{R}_{N_S})$. For the sake of simplicity, we have not attempted to compute this Skyrmion generalized elastic energy from the full non-linear sigma model. We postulate a simple phenomenological form, which is based on the fact that each Skyrmions carries a fundamental electric charge e, interacting with the laws of electrostatics. Typically, we set:

$$V_{\rm el}(\boldsymbol{R_1}, ..., \boldsymbol{R_{N_S}}) = \tau \sum_{i=1}^{N_S} V_{\rm ext}(\boldsymbol{R}_i) + \frac{e^2}{2\epsilon l_B} \sum_{<i,j>} \frac{1}{(|\boldsymbol{R}_i - \boldsymbol{R}_j|^2 + 1)^{1/2}} \tag{19}$$

As above, positions are expressed in units of the magnetic length l_B. Here, $\tau = 1$ (resp. $\tau = -1$) for negatively (resp. positively) charged Skyrmions. The inter-Skyrmion Coulomb potential is expected to be regular at small separation, which motivates the above modification of the bare Coulomb potential at short distances. To simplify the numerical calculations, we will also keep only the Coulomb repulsion between nearest neighbor Skyrmions. The magnon dynamics in the presence of N_S Skyrmions is assumed to take the same form as before, but in the magnon Hamiltonian (15), both the effective gauge field $\boldsymbol{A}$ and the local potential $V_{\rm loc}$ depend on the Skyrmion positions. Again, we do not attempt to extract them from a full calculation, but postulate the phenomenological forms:

$$\boldsymbol{\nabla} \times \boldsymbol{A}(\boldsymbol{r}) = \sum_{i=1}^{N_S} \frac{4a^2}{(|\boldsymbol{r} - \boldsymbol{R_i}|^2 + a^2)^2} \tag{20}$$

$$V_{\rm loc}(\boldsymbol{r}) = V_{\rm ext}(\boldsymbol{r}) + \tau \frac{e^2}{\epsilon l_B} \sum_{i=1}^{N_S} \frac{1}{(|\boldsymbol{r} - \boldsymbol{R}_i|^2 + b^2)^{1/2}} \tag{21}$$

Here a and b are positive length scales of the order of the magnetic length. For a qualitative phenomenological modelling of the electrostatic potential of the junction we shall assume that V_{ext} comprises a hard-wall along the y-axis potential beyond a certain junction length, and a quadratic potential along the x-axis, which flattens out to a constant beyond the width of the junction. We present the details and results of such a phenomenological approach in the next section.

Equations of motion for Skyrmion positions can be derived by restricting the symplectic form generating Hamilton's equations of motion from the infinite-dimensional family of smooth maps $\boldsymbol{n}(\boldsymbol{r})$ to the finite sub-manifold of low energy configurations $\boldsymbol{n}(\boldsymbol{r}; \boldsymbol{R}_1, ...\boldsymbol{R}_{N_S})$ parametrized by the Skyrmion positions. The symplectic form Ω is defined as follows: for two infinitesimal deformations $\boldsymbol{\xi}_1(\boldsymbol{r})$, $\boldsymbol{\xi}_2(\boldsymbol{r})$ around $\boldsymbol{n}(\boldsymbol{r})$ (so $\boldsymbol{n}(\boldsymbol{r}).\boldsymbol{\xi}_i(\boldsymbol{r}) = 0$, $i = 1, 2$),

$$\Omega_{\{\boldsymbol{n}\}}(\boldsymbol{\xi}_1, \boldsymbol{\xi}_2) = \int \frac{d^2\boldsymbol{r}}{4\pi l_B^2}\, \boldsymbol{n} \cdot (\partial_x \boldsymbol{\xi}_1 \times \partial_y \boldsymbol{\xi}_2) \tag{22}$$

Let us now consider two infinitesimal variations $\delta\boldsymbol{R}_i^{(1)}$ and $\delta\boldsymbol{R}_i^{(2)}$ of the Skyrmion positions. This gives rise to $\boldsymbol{\xi}_1(\boldsymbol{r})$ and $\boldsymbol{\xi}_2(\boldsymbol{r})$ according to:

$$\boldsymbol{\xi}_{1,2}(\boldsymbol{r}) = \sum_{i=1}^{N_S} \sum_{a=x,y} \frac{\partial \boldsymbol{n}}{\partial \boldsymbol{R}_i^a}\, \delta\boldsymbol{R}_i^{a,(1,2)} \tag{23}$$

Substituting in the above expression for the symplectic form, we get a complicated expression, that we may approximate assuming that Skyrmions do not overlap much. As a first consequence, we can neglect off-diagonal terms of the form $\delta\boldsymbol{R}_i^{a,(1)}\, \delta\boldsymbol{R}_j^{b,(2)}$ with $i \neq j$. While evaluating the $\boldsymbol{r}$ integral, the prefactor of the $\delta\boldsymbol{R}_i^{x,(1)}\, \delta\boldsymbol{R}_i^{y,(2)}$ term is dominated by the region where $\boldsymbol{r}$ is closer to $\boldsymbol{R}_i$ than to $\boldsymbol{R}_j$ for $j \neq i$. In this region, we have an approximate invariance for $\boldsymbol{n}(\boldsymbol{r}; \boldsymbol{R}_1, ...\boldsymbol{R}_{N_S})$ under infinitesimal translations that are acting only on $\boldsymbol{r}$ and $\boldsymbol{R}_i$. Therefore, we can replace $\frac{\partial \boldsymbol{n}}{\partial \boldsymbol{R}_i^a}$ by $-\frac{\partial \boldsymbol{n}}{\partial \boldsymbol{r}^a}$, so we simply get the topological charge associated to a Skyrmion. With this approximation, the reduced symplectic form reads:

$$\Omega_{\rm red}(\{\delta\boldsymbol{R}_i^{(1)}\}, \{\delta\boldsymbol{R}_i^{(2)}\}) = \frac{\tau}{l_B^2} \sum_{i=1}^{N_S} (\delta\boldsymbol{X}_i^{(1)}\, \delta\boldsymbol{Y}_i^{(2)} - \delta\boldsymbol{X}_i^{(2)}\, \delta\boldsymbol{Y}_i^{(1)}) \tag{24}$$

Hamiltonian equations for motion for the skyrmions take then the familiar form

$$\dot{X}_i = \tau \frac{l_B^2}{\hbar} \frac{\partial H}{\partial Y_i}, \quad \dot{Y}_i = -\tau \frac{l_B^2}{\hbar} \frac{\partial H}{\partial X_i} \tag{25}$$

As for the magnon, it will be convenient to use l_B as the unit length for Skyrmion positions, so that l_B disappears in these evolution equations. We emphasize the qualitative difference between the magnon and the Skyrmions from the viewpoint of their symplectic forms. Because the magnon is a charge neutral object, its phase-space is four-dimensional, described by the $\boldsymbol{r}, \boldsymbol{p}$ coordinates. By contrast, Skyrmions carry one unit charge, so the corresponding phase-space is two-dimensional and is identified to the physical plane for $\boldsymbol{R}_i$.

To summarize, we have reduced the infinite-dimensional phase-space of the non-linear sigma model to a phase-space of dimension $4 + 2N_S$ for one magnon coupled to N_S Skyrmions. The Hamiltonian generating the time-evolution of

this system is $H = H_{\rm mag} + V_{\rm el}$, with $H_{\rm mag}$ given by Eq. (15) and $V_{\rm el}$ by Eq. (19). The corresponding equations of motion for the magnon are given by (16) and those for Skyrmions by (25). We note that when Skyrmions are moving, in particular as the result of their interaction with an incoming magnon, there is an induced electromotive force acting on the magnon, since it experiences a time-dependent effective vector potential. In the numerical simulations inspired by the present model, we have neglected these induction phenomena, on the basis that Skyrmions are slowly moving. It is an interesting direction for future work to explore the consequences of (relaxing) this simplifying assumption.

Phenomenological model involving charged particle in a flux-tube array

In the previous section, we have presented a complete semiclassical description of the magnon-skyrmion crystal junction problem, deriving equations of motion for both the magnons and the skyrmions. We expect such an analytical treatment to be a starting point for several other such similar situations of magnons interacting with quantum Hall type insulators with non-trivial topology.

In the absence of exact information about junction parameters, we have also postulated several forms of the electrostatic potentials and effective magnetic fields based on physical arguments and approximations. Here we shall summarize the full phenomenological setup and explain the numerical procedure for obtaining the magnon trajectories and variance.

Based on the above sections illustrating the equivalence of different microscopic pictures and appropriate semiclassical limits, here we present the details of the simplest phenomenological model which qualitatively captures the sharp noise feature across all detectors in narrow voltage windows. We show that shaking of the skyrmion crystal by the magnons, when the crystal softens, is the source for the linearly increasing (with voltage) variance in the non-local magnon signal across all detectors.

The crucial ingredients of the phenomenological model are :

i) the two confining potentials along x and y which constitute $V_{ext}(\boldsymbol{r})$. For the former we use a quadratic potential, $V_{cx} = K_x x^2/(1 + (x/x_0)^2)$ for the junction width, which smoothly saturates to a constant, $K_x x_0^2$, away from the junction for $x \gg x_0$. For the latter, we use a flat potential $V_{cy} = 0$, along the junction region and a hard-wall, $V_{cy} = K_y(|y| - y_J)^4$ form, beyond the junction.

ii) The electrostatic potential induced in the junction region by the skyrmion, for which we use the form presented in the second term of eq. (21).

iii) The effective magnetic field induced by the skrymion crystal's modulated topological charge density. We take this to have the $B(\boldsymbol{r} - \boldsymbol{R})$ to have the form presented in eq. 20.

iv) The repulsive nearest neighbour inter-skyrmion potential, which we take to be of the form in the second term of eq. 19. Note that the first term is the same V_{ext} as in point (i) above, but now for the skyrmion coordinates.

These ingredients are all the inputs required to numerically solve the equations of motion for the magnon (eq. 18) and the skyrmions (eq. 25). Let us write these down more explicitly to clearly see the different terms induced by the different factors. First, we focus on the skyrmions, the Hamiltonian for which is given by $H = H_{mag} + V_{el}$. While the second term will give us the standard potential derivatives, the dependence of the first term on the skyrmion coordinates results in the magnon recoil induced collective dynamics. Recall that skyrmion centre coordinates are denoted as X_i, Y_i and magnon position and momenta are denoted as x, y and p_x, p_y respectively. We can write

$$\begin{aligned}
\frac{\partial H_{mag}}{\partial Y_i} = \frac{\omega_{int}}{2}\Big[-2(p_x - A_x)\frac{\partial A_x}{\partial Y_i} - 2(p_y - A_y)\frac{\partial A_y}{\partial Y_i}\Big] + (p_x - A_x)\partial_{Y_i}\partial_y V_{loc} - (\partial_y V_{loc})(\frac{\partial A_x}{\partial Y_i}) \\
- (p_y - A_y)\partial_{Y_i}\partial_x V_{loc} + (\partial_x V_{loc})(\frac{\partial A_y}{\partial Y_i}) \\
\frac{\partial H_{mag}}{\partial X_i} = \frac{\omega_{int}}{2}\Big[-2(p_x - A_x)\frac{\partial A_x}{\partial X_i} - 2(p_y - A_y)\frac{\partial A_y}{\partial X_i}\Big] + (p_x - A_x)\partial_{X_i}\partial_y V_{loc} - (\partial_y V_{loc})(\frac{\partial A_x}{\partial X_i}) \\
- (p_y - A_y)\partial_{X_i}\partial_x V_{loc} + (\partial_x V_{loc})(\frac{\partial A_y}{\partial X_i}) \qquad (26)
\end{aligned}$$

These set of formulae, combined with the standard potential derivatives of V_{el} form the equations of motion for the skyrmions. To proceed with the calculations, we choose the Landau gauge with $A_x = 0$ and $A_y = \sum_{i=1}^{N_S}(x - X_i)B_{\boldsymbol{r'R_i}}$

where $B_{\boldsymbol{r'R_i}} = 4a^2/(|\boldsymbol{r'} - \boldsymbol{R_i}|^2 + a^2)^2$ as in eq. (20). As a consequence we get

$$\begin{aligned} \frac{\partial A_y}{\partial x} &= \sum_{i=1}^{N_S} B_{\boldsymbol{r'R}_i} = B; \frac{\partial A_x}{\partial y} = \frac{\partial A_x}{\partial X_i} = \frac{\partial A_x}{\partial Y_i} = 0 \\ \frac{\partial A_y(x,y,\boldsymbol{X},\boldsymbol{Y})}{\partial X_i} &= -B_{\boldsymbol{r},\boldsymbol{R}_i} \\ \frac{\partial A_y(x,y,\boldsymbol{X},\boldsymbol{Y})}{\partial Y_i} &= (x - X_i)\frac{\partial B_{\boldsymbol{r},\boldsymbol{R}_i}}{\partial Y_i} = \frac{16a^2(x-X_i)(y-Y_i)}{(|\boldsymbol{r} - \boldsymbol{R}_i|^2 + a^2)^3} \end{aligned} \tag{27}$$

In a similar vein we rewrite the magnon equations of motion.

$$\begin{aligned} \ddot{x} &= (\omega_{int}B + \partial_x^2 V_{loc} + \partial_y^2 V_{loc})\dot{y} + (\partial_y V_{loc})(\partial_x \partial_y V_{loc}) + (\partial_x V_{loc})(\partial_x^2 V_{loc}) \\ \ddot{y} &= -(\omega_{int}B + \partial_x^2 V_{loc} + \partial_y^2 V_{loc})\dot{x} + (\partial_y V_{loc})(\partial_y^2 V_{loc}) + (\partial_x V_{loc})(\partial_y \partial_x V_{loc}) \end{aligned} \tag{28}$$

where B is the total magnetic field generated by all the skyrmions. We clearly see that the variation of the electrostatic potential (also modified by the skyrmions) contributes an effective Lorentz force as well as a scalar potential. The various derivatives of the electrostatic potential felt by the magnons also act as sources of effective magnetic field and scalar potentials as highlighted in the above sections. They are given by

$$\begin{aligned} \partial_x V_{loc} &= \partial_x V_{cx} - \sum_{i=1}^{N_S} \frac{(x - X_i)}{(|\boldsymbol{r} - \boldsymbol{R}_i|^2 + b^2)^{3/2}}; \partial_y V_{loc} = \partial_y V_{cy} - \sum_{i=1}^{N_S} \frac{(y - Y_i)}{(|\boldsymbol{r} - \boldsymbol{R}_i|^2 + b^2)^{3/2}} \\ \partial_{X_i}\partial_x V_{loc} &= \frac{1}{(|\boldsymbol{r} - \boldsymbol{R}_i|^2 + b^2)^{3/2}} - \frac{3(x - X_i)^2}{(|\boldsymbol{r} - \boldsymbol{R}_i|^2 + b^2)^{5/2}}; \partial_{Y_i}\partial_y V_{loc} = \frac{1}{(|\boldsymbol{r} - \boldsymbol{R}_i|^2 + b^2)^{3/2}} - \frac{3(y - Y_i)^2}{(|\boldsymbol{r} - \boldsymbol{R}_i|^2 + b^2)^{5/2}}; \\ \partial_{Y_i}\partial_x V_{loc} &= \partial_{X_i}\partial_y V_{loc} = \frac{-3(x - X_i)(y - Y_i)}{(|\boldsymbol{r} - \boldsymbol{R}_i|^2 + b^2)^{5/2}} \end{aligned} \tag{29}$$

We find it quite striking that the magnon-skyrmion crystal model, when captured within this non-linear sigma model so clearly elucidates the interplay of topology, geometry and collective dynamics. We hope that such analytical analysis serves as a starting point for similar magnon based probes of other topological phases of matter.

We numerically solve the above equations of motion to obtain the magnon and skyrmion trajectories. We consider the magnons to be scattered, one by one, with an initial velocity $\boldsymbol{v}$ and incidence angle θ_i. These equations form the basis of our phenomenological model, which we then numerically solve using standard symplectic mid-point integration techniques. We start with a 5 skyrmion, lined along the y-axis range in the central region around x = 0. Now we consider charged particles starting at $x = -L$ and at a random point in the $y = [-4, 4]$ range. We do so to simulate emission from the central detector at the end of the left slab, as is done for the noise data in the experiment. For Fig. 4C in the main text, we simulate a total of 10000 magnons starting from the initial conditions described above, with $dt = 0.001$ time step in our midpoint Strang symplectic integration scheme and we vary the number of steps per pass to simulate the varying magnon flux. To obtain the variance data shown in Fig. 4C, we define a suitable unit of time and simply obtain the number of charged particles that hit each of the detectors (three different y coordinate ranges at x = +L) in that unit of time. This is the magnon count, also illustrated in Fig 3D and E. Further, we model the reduced stiffness by reducing the coefficient of the x-axis confining potential K_x. As shown in Fig. S8, a reduction in stiffness drastically increases the noise in the skyrmion positions.

Our results lend qualitative support to the picture that, dynamics of the skyrmion crystal induced by the impinging magnons is the cause for the sharp noise observed in the experiment at periodic voltages corresponding to the discrete process of adding an extra skyrmion. Within our simple model this can be illustrated clearly, as in Fig. S8, by explicitly looking at the trajectories of the flux tubes and their deflection when a charged particle passes by.

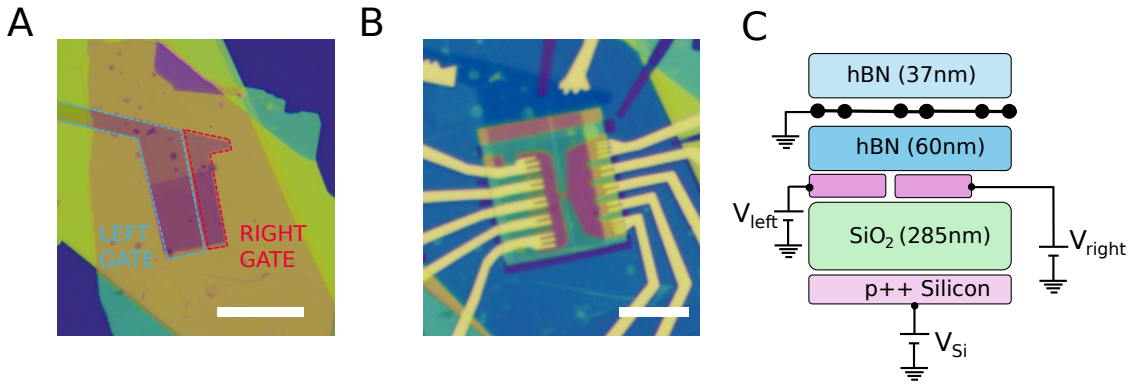

FIG. S1. (a) Optical image of the hBN/graphene/hBN/graphite stack (top to bottom). The bottom graphite was pre-patterned into two gates shown in dashed red (left gate) and blue (right gate), respectively. Scale bar is 5 μm. The separation between left and right gates is ∼70 nm. (b) Optical image of the final device. Scale bar is 5 μm. (c) Cross-sectional schematic of the device. right-gate voltage (V_{right}) and left-gate voltage (V_{left}) were applied to the two graphite gates as shown. These two gates are separated by ∼70 nm.

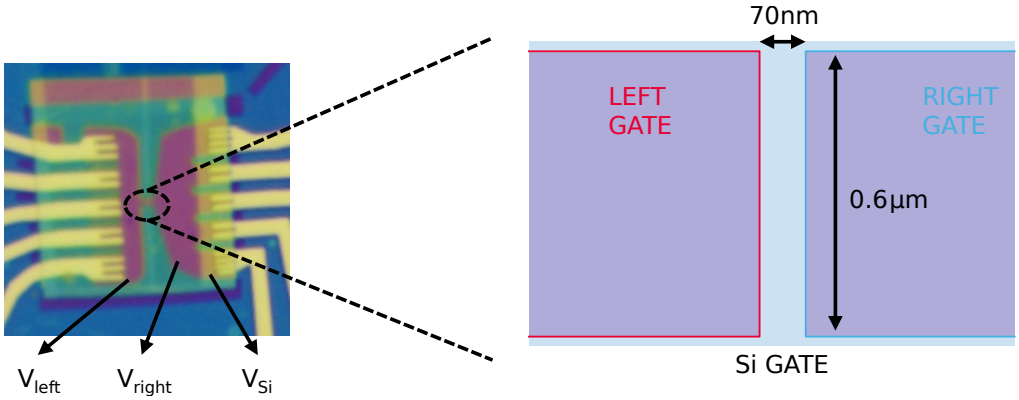

FIG. S2. Optical image of the device showing the details of the constriction and the gate configuration. The width of the graphene channel and the gates is 0.6 μm, and the distance between left and right gates is 70 nm.

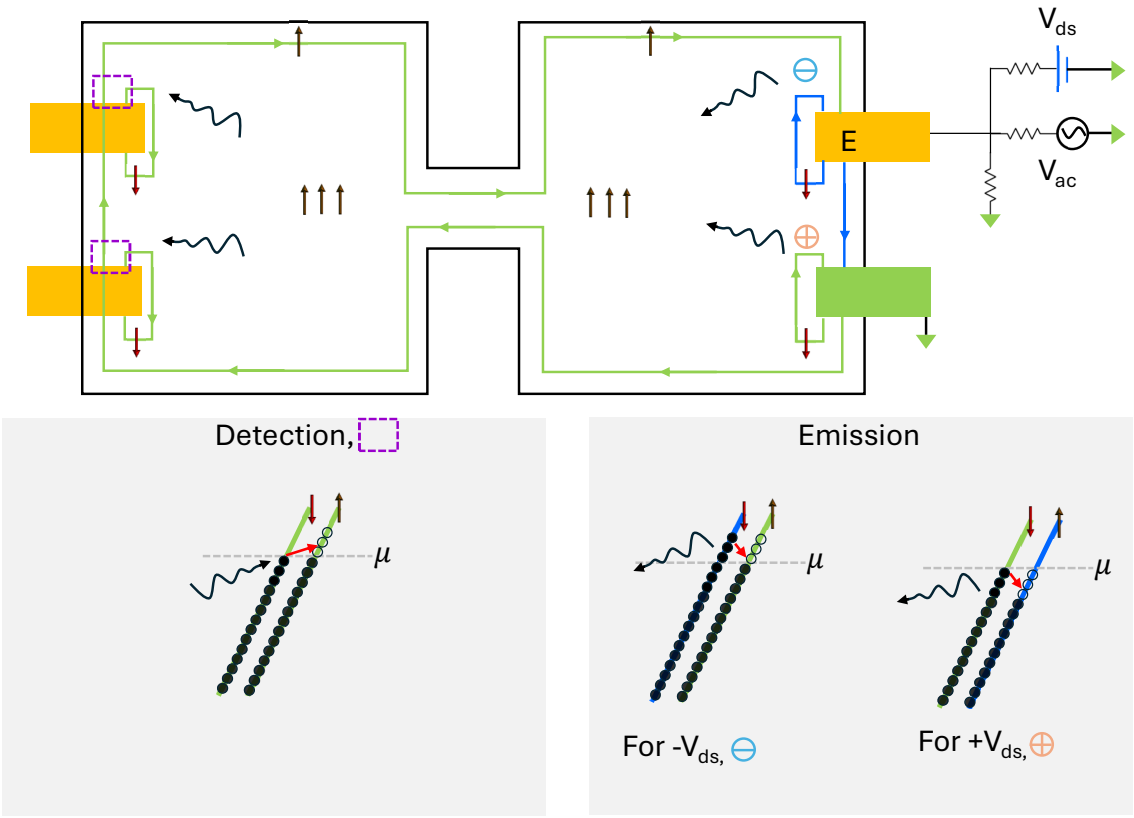

FIG. S3. **Top panel**: Schematic of the measurement setup used in this experiment. **Bottom panel**: Edge-state illustration of magnon emission and absorption processes. The symbols ⊖ and ⊕ denote the locations where magnons are emitted for negative and positive V_{ds}, respectively.

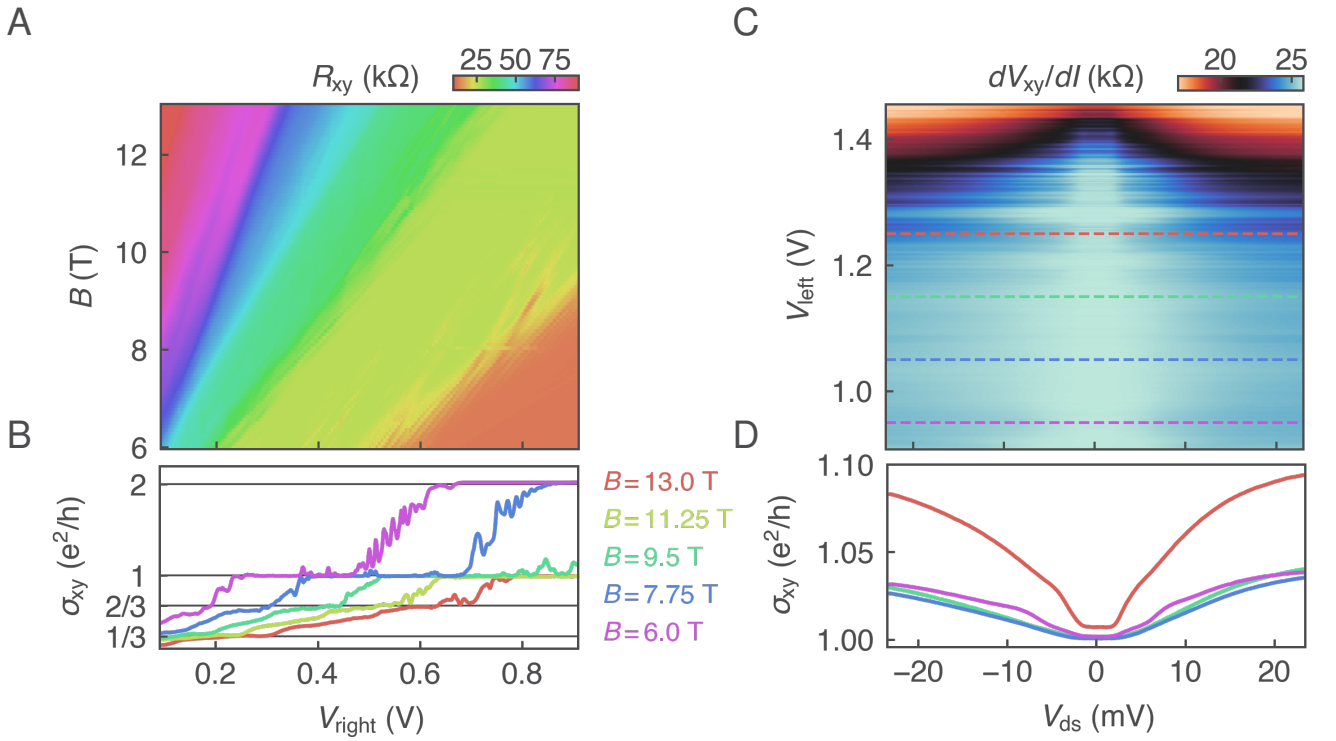

FIG. S4. **(a)** Landau fan of the two-terminal Hall resistance R_{xy} measured from 6 to 13 T while sweeping the right gate voltage. A contact resistance of 750 Ω, corresponding to the series resistance of the device contacts, has been subtracted. Well-quantized plateaux are observed at $\sigma = e^2/h$, $2e^2/h$, $1/3, e^2/h$, and $2/3, e^2/h$, demonstrating the high sample quality and the presence of robust integer and fractional quantum Hall states. **(b)** Line cuts of R_{xy} at fixed magnetic fields (6, 7.75, 9.5, 11.25, and 13 T), illustrating the persistence and sharpness of both integer and fractional plateaux across the full field range. **(c)** Breakdown of the $\nu = 1$ quantum Hall state as a function of source–drain bias. A small reduction of 2.5–8% at $V_{\mathrm{ds}} = 20$ mV signals the onset of dissipative processes, preceding the full collapse of the plateau at higher bias. **(d)** Representative bias-dependent cuts illustrating the full breakdown of the $\nu = 1$ plateau.

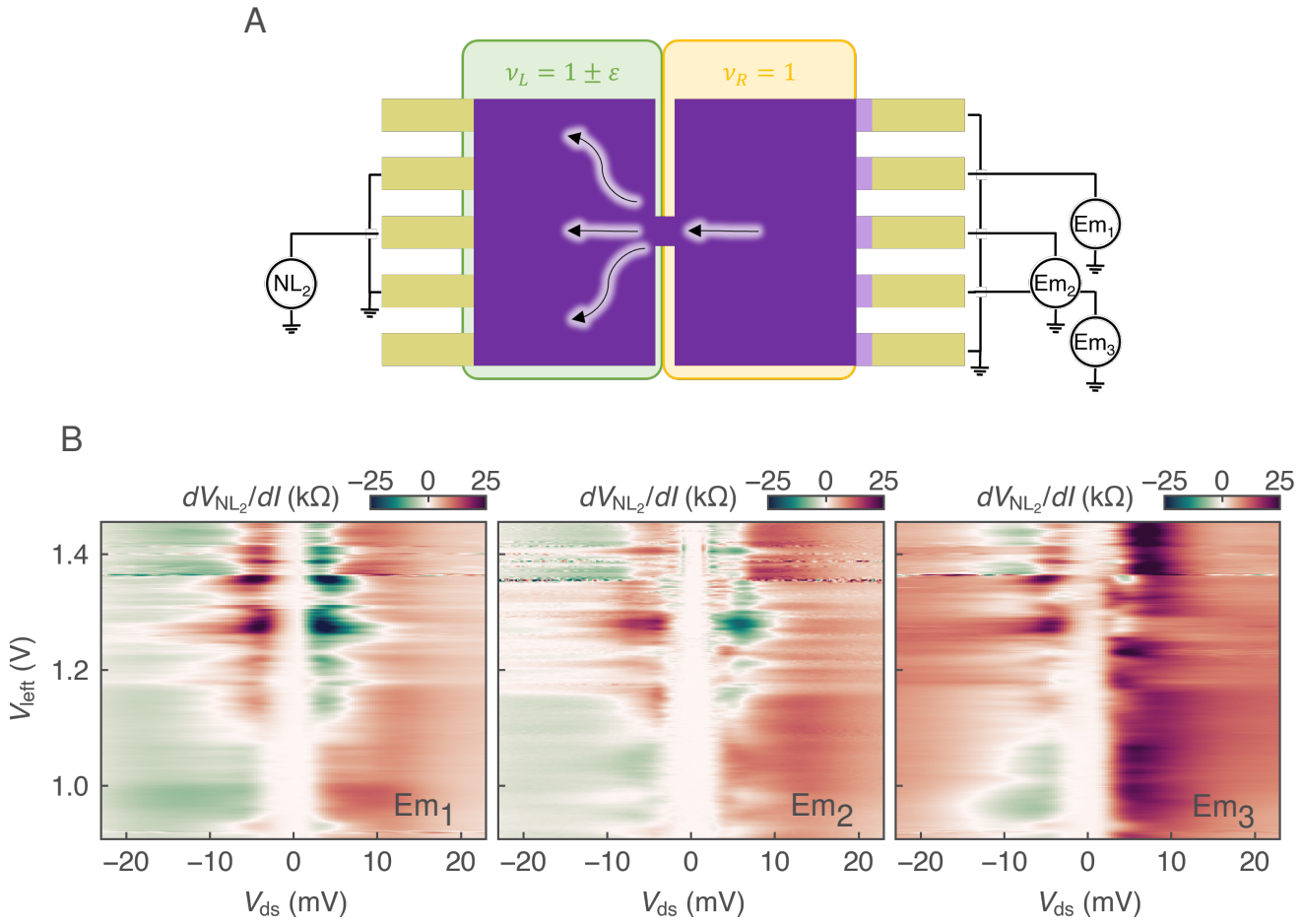

FIG. S5. **(a)** Schematic of the experimental geometry showing the three magnon emitters, $E_{m,1}$, $E_{m,2}$, and $E_{m,3}$, positioned at different lateral angles with respect to the gated junction region. Magnons emitted from these contacts propagate toward the junction, where they interact with the in-plane electric field and experience momentum-dependent scattering before reaching the nonlocal detector NL2. **(b)** Nonlocal magnon signals dV_{NL}/dI measured at NL2 for each of the three emitters. The lateral emitters produce a substantially stronger response due to their larger transverse momentum components, which enhance the coupling between the magnon electric dipole and the in-plane electric field, leading to increased scattering and redirection toward NL2. In contrast, magnons injected from the central emitter $E_{m,2}$ predominantly follow near-normal trajectories across the junction and couple more weakly to the electric field, resulting in a comparatively smaller nonlocal signal.

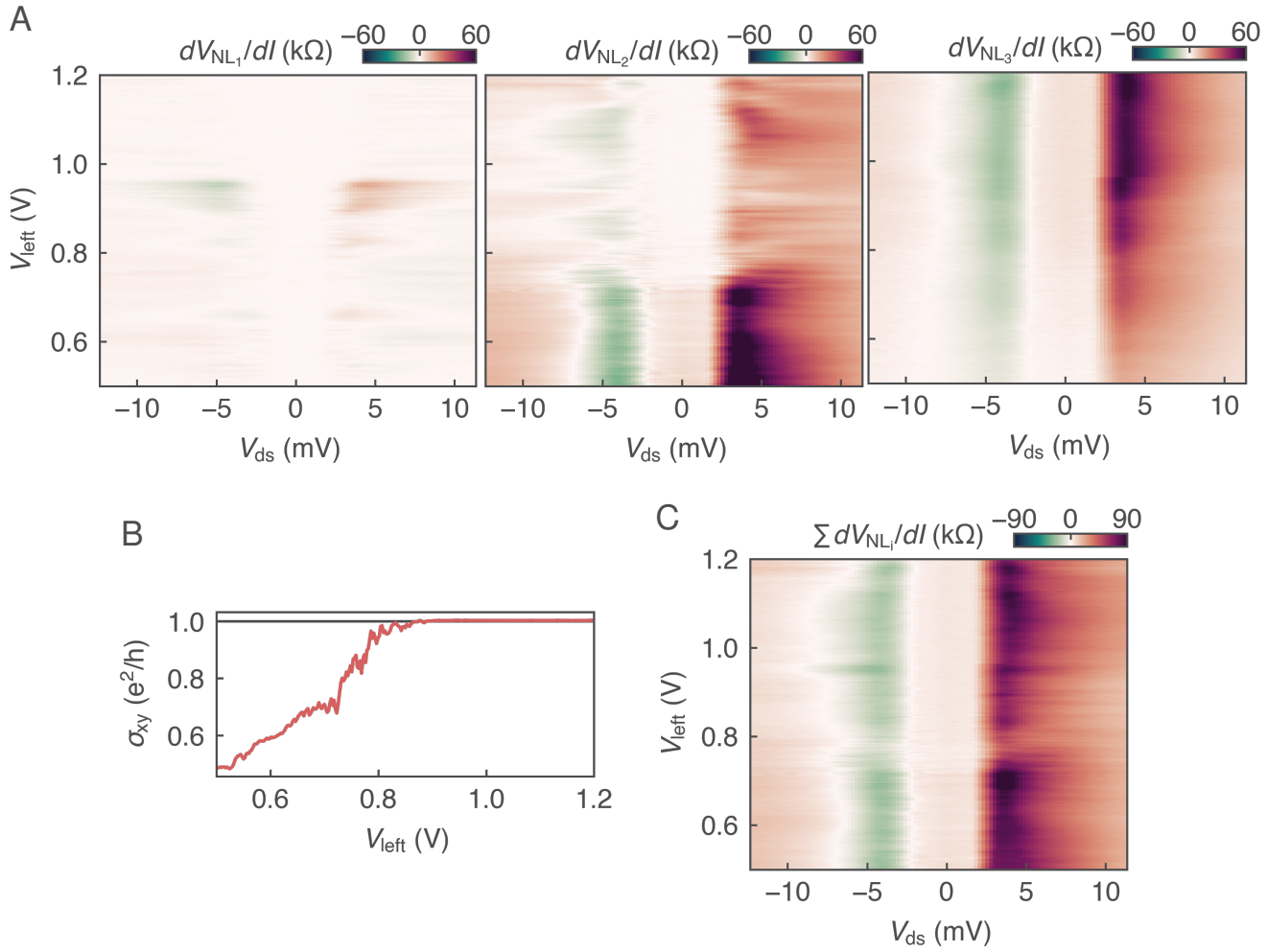

FIG. S6. **(a)** Non-local magnon signals measured at detectors NL1, NL2, and NL3 while exciting the central emitter $E_{m,2}$. Each trace corresponds to a single detector, showing the distribution of the magnon signal across the device. **(b)** Simultaneously measured Hall conductivity σ_{xy} in the right-gated region. **(c)** Total integrated magnon signal summed over all three detectors. The signal remains approximately constant across the range of carrier densities studied, demonstrating conservation of the magnon flux through the bulk despite small variations in individual detector amplitudes. No distinctive skyrmion-crystal signatures are observed from this measurement perspective.

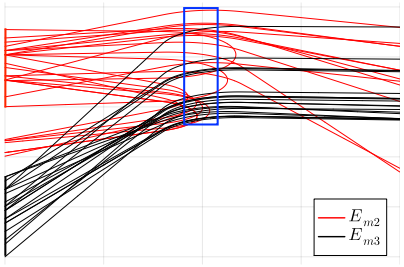

FIG. S7. Magnon trajectories in the absence of any skyrmions in the junction (blue box). As mentioned in the text, the electrostatic confining potential profile in the junction generates an effective Lorentz force and a scalar potential due to the drift velocity. As a consequence, even in the absence of skyrmions the magnon trajectories are deflected. More importantly, magnons impinging at a greater angle are deflected more towards the central detector as compared to those emitted from the central emitter (bold red). See text for the form of the electrostatic potential. This explains the observations of the experiment in Fig. S5 and validates the relation of our modelling with the dipole moment picture. Also note that this clearly demonstrates that the drastic reduction of a magnon signal at a central detector *cannot* be considered as evidence of any skyrmions or inelastic processes, as such a reduction can be purely due to electric field effects in the central region.

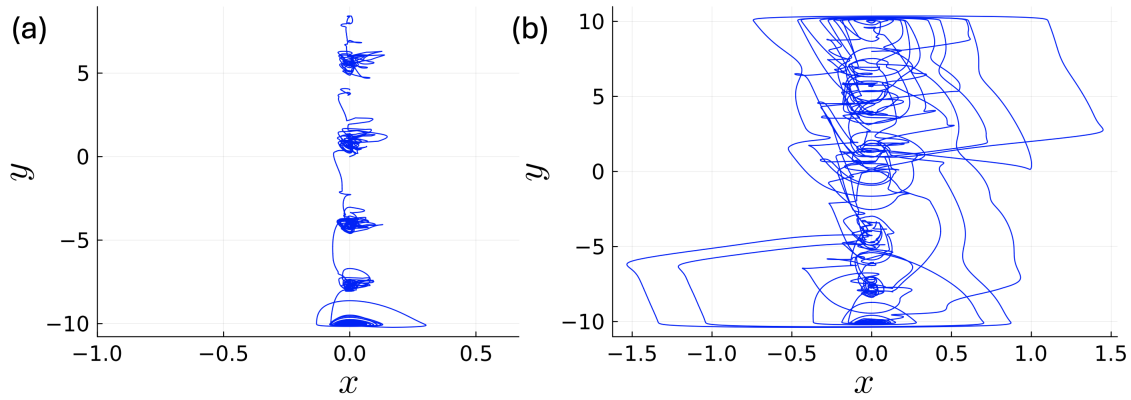

FIG. S8. Skyrmion centre positions for high (a) and low (b) stiffness altered through shaking by magnons. We see that for different values of K_x, the degree to which the impinging magnons alters the collective motion of the crystal varies drastically.

[1] C. Kallin and B. I. Halperin, Phys. Rev. B **30**, 5655 (1984).
[2] S. L. Sondhi, A. Karlhede, S. A. Kivelson, and E. H. Rezayi, Phys. Rev. B **47**, 16419 (1993).
[3] K. Moon, H. Mori, K. Yang, S. M. Girvin, A. H. MacDonald, L. Zheng, D. Yoshioka, and S.-C. Zhang, Phys. Rev. B **51**, 5138 (1995).
[4] N. Chakraborty, R. Moessner, and B. Doucot, Phys. Rev. B **108**, 104401 (2023).